MASARYKOVA UNIVERZITA
PŘÍRODOVĚDECKÁ FAKULTA
ÚSTAV FYZIKY A TECHNOLOGIÍ PLAZMATU

Bakalářská práce

BRNO 2026 LUKÁŠ LEJDAR

MASARYKOVA
UNIVERZITA
PŘÍRODOVĚDECKÁ FAKULTA
ÚSTAV FYZIKY A TECHNOLOGIÍ PLAZMATU

Numerické modelování rozložení elektrického pole a Jouleova ohřevu v plazma-kapalinových reaktorech metodou konečných prvků

Bakalářská práce

Lukáš Lejdar

Vedoucí práce: Mgr. Zdeněk Bonaventura, Ph.D. **Brno 2026**

Bibliografický záznam

Autor:	Lukáš Lejdar Přírodovědecká fakulta, Masarykova univerzita Ústav fyziky a technologií plazmatu
Název práce:	Numerické modelování rozložení elektrického pole a Jouleova ohřevu v plazma-kapalinových reaktorech metodou konečných prvků
Studijní program:	Fyzika
Studijní obor:	Fyzika
Vedoucí práce:	Mgr. Zdeněk Bonaventura, Ph.D.
Akademický rok:	2025/2026
Počet stran:	xvi + 38
Klíčová slova:	plazma–kapalina; elektrický výboj; konečné prvky; numerická simulace; Jouleovo teplo; vodivost vody; elektrostatický model

Bibliographic Entry

Author:	Lukáš Lejdar Faculty of Science, Masaryk University Department of Plasma Physics and Technology
Title of Thesis:	Numerical Modelling of Electric Field Distribution and Joule Heating in Plasma–Liquid Reactors using Finite Elements
Degree Programme:	Physics
Field of Study:	Physics
Supervisor:	Mgr. Zdeněk Bonaventura, Ph.D.
Academic Year:	2025/2026
Number of Pages:	xvi + 38
Keywords:	plasma–liquid; electrical discharge; finite element method; numerical simulation; Joule heating; water conductivity; electrostatic model

Abstrakt

Tato práce se zabývá numerickým modelováním elektrického pole v reaktoru pro generaci plazmového výboje na rozhraní vody a vzduchu. Hlavním cílem je vytvoření elektrostatického modelu založeného na metodě konečných prvků a analýza elektrických vlastností reaktoru pro deionizovanou a kohoutkovou vodu.

Nejprve jsou odvozeny slabé a smíšené formulace Poissonovy rovnice a následně je představena jejich diskretizace pomocí vhodných konečněprvkových prostorů. Zvláštní pozornost je věnována Raviartovým–Thomasovým prvkům, které umožňují zachovat spojitost normálové složky elektrického posuvného pole a lokální zákony zachování.

Dále jsou z numerického modelu určeny ekvivalentní parametry elektrického obvodu reaktoru, zejména odpor a kapacita. Výsledky jsou porovnány s experimentálními měřeními proudových průběhů publikovanými v literatuře. Na závěr je diskutována energie uložená do systému během pulzu a význam odporového ohřevu ve srovnání s energií samotného plazmového výboje.

Abstract

This work deals with numerical modeling of the electric field in a reactor used for plasma discharge generation at the water–air interface. The main goal is the development of an electrostatic model based on the finite element method and the analysis of the electrical properties of the reactor for deionized and tap water.

First, weak and mixed formulations of the Poisson equation are derived, followed by their discretization using suitable finite element spaces. Special attention is devoted to Raviart–Thomas elements, which preserve continuity of the normal component of the electric displacement field and ensure local conservation properties.

The equivalent circuit parameters of the reactor, in particular the resistance and capacitance, are then determined from the numerical model. The results are compared with experimentally measured current waveforms reported in the literature. Finally, the deposited pulse energy and the role of resistive heating are discussed in comparison with the energy released by the plasma discharge itself.

MUNI
SCI

MASARYKOVA UNIVERZITA
PŘÍRODOVĚDECKÁ FAKULTA
KOTLÁŘSKÁ 2, 611 37 BRNO
IČ: 00216224
DIČ: CZ00216224

ZADÁNÍ BAKALÁŘSKÉ PRÁCE

Akademický rok: 2025/2026

Ústav:	Ústav fyziky a technologií plazmatu
Student:	Lukáš Lejdar
Program:	Fyzika
Specializace:	Fyzika

Ředitel *ústavu* PřF MU Vám ve smyslu Studijního a zkušebního řádu MU určuje bakalářskou práci s názvem:

Název práce:	Numerické modelování rozložení elektrického pole a Jouleova ohřevu v plazma-kapalinových reaktorech metodou konečných prvků
Název práce anglicky:	Numerical Modelling of Electric Field Distribution and Joule Heating in Plasma–Liquid Reactors using Finite Elements
Jazyk práce:	angličtina

Oficiální zadání:

Non-equilibrium (or cold) plasma is particularly effective at generating reactive species under conditions where the bulk gas temperature remains low, yet the electrons are highly energetic. One common way to create such plasmas is through streamer-spark discharges, which are initiated by strong electric fields from microsecond pulsed power sources. In these discharges, fast-moving ionization fronts (streamers) quickly propagate through the gas, producing a variety of chemically active species, before forming sparks when the streamer channels transit into a more conductive phase. Efficiently delivering plasma-generated reactive species into a liquid involves complex chemistry and physics at the gas–water interface. Here, molecules and radicals must navigate sudden changes in medium—passing from a highly energized, non-equilibrium plasma environment into a comparatively stable liquid phase. This transition is not only influenced by fluid properties (e.g., density, viscosity, surface tension) but also by rapid chemical reactions that can either consume or transform the reactive species before they even reach the liquid bulk. Because these processes unfold under strongly non-equilibrium conditions, where electron energies and temperature gradients vary drastically over very short (often nanosecond) timescales, traditional equilibrium-based models for the interface particle transfer fail to capture the full picture.

Thus, an accurate understanding of how reactive species form, diffuse, and ultimately dissolve in the liquid demands advanced experimental techniques—for instance, time-resolved optical spectroscopy, laser-induced fluorescence, or high-speed imaging—that can track changes in real time and at high spatial resolution. Complementing these methods with state-of-the-art multi-physics numerical models, which incorporate detailed plasma and liquid phase reaction kinetics, heat transfer, interfacial physics (including mass transfer due to moving liquid and surface agitation), enables us to go beyond simplified assumptions.

This bachelor thesis aims to develop a robust numerical model for electric field distribution within the reactor considering real reactor geometry simplified to 2D. Moreover, based on the obtained spatial distribution of the electric field, a numerical model for Joule heating of water flowing through the reactor should be developed. Preferred numerical framework for this bachelor thesis is the Finite Element Method, allowing for easy coupling of multiphysis models, praticularly the deal.II Finite Element Library is recommended.

Vedoucí práce:	Mgr. Zdeněk Bonaventura, Ph.D.
Datum zadání práce:	6. 11. 2025
V Brně dne:	10. 5. 2026

Lukáš Lejdar, 18. 12. 2025
Mgr. Zdeněk Bonaventura, Ph.D., 19. 12. 2025
RNDr. Luboš Poláček, 31. 3. 2026

Poděkování

Na tomto místě bych chtěl poděkovat svému vedoucímu Mgr. Zdeňku Bonaventurovi, Ph.D., za jeho věnovaný čas, cenné připomínky a zajímavé diskuze během psaní této práce.

Prohlášení

Prohlašuji, že jsem svoji bakalářskou práci vypracoval samostatně pod vedením vedoucího práce s využitím informačních zdrojů, které jsou v práci citovány.

Brno 13. května 2026 .....

Lukáš Lejdar

Contents

Introduction **1**

Chapter 1. Physical model of the discharge **3**
1.1 Reactor geometry and experimental configuration 3
1.2 Reference experimental data 4
1.3 Physical processes relevant for numerical modelling 5
1.3.1 Electrostatic approximation 5
1.3.2 Equivalent electrical model 6
1.3.3 Surface charge formation 8
1.3.4 Joule heating in the liquid phase 8

Chapter 2. Finite element method **9**
2.1 Weak formulation 9
2.2 Finite element discretization 10
2.3 Mixed formulation 11
2.4 Convergence and Error Estimation 12
2.4.1 A Priori Error Estimates 12
2.4.2 A Posteriori Error Estimation 14

Chapter 3. Implementation **15**
3.1 Geometry and Meshing 15
3.2 Test case for the numerical method 19
3.2.1 Test case definition 19
3.2.2 Test case convergence study 20
3.2.3 Adaptive refinement 21

Chapter 4. Computation and Results **25**
4.1 Physical Parameters and Boundary Conditions 25
4.1.1 Numerical results and comparison with measurement 25
4.1.2 Equivalent circuit parameters 28
4.1.3 Heating model 29
4.2 Convergence and error analysis 30
4.2.1 Anisotropic adaptive refinement 31

Chapter 5. Conclusion **35**

Introduction

Electrical discharges generated at atmospheric pressure are widely studied because of their ability to efficiently produce chemically reactive species under relatively low gas temperatures [1], [2]. In recent years, there was a lot of attention given to plasma–liquid systems, in which plasma interacts directly with a liquid surface. These systems are investigated for applications including water treatment, plasma agriculture, plasma–assisted chemistry, and plasma–activated liquids [1], [3].

This thesis focuses on a nanosecond pulsed discharge propagating along a air–water interface in a dielectric barrier discharge reactor geometry introduced experimentally by Hoffer et al. [4] and later studied in greater detail by Arora et al. [5].

The main objective of this thesis is the construction of a numerical model of the experimental reactor and the solution of the corresponding electrostatic problem using the finite element method. Using the model we will construct a simple equivalent circuit model of the reactor and estimate Joule heating generated by conductive currents flowing through the liquid phase.

The remainder of this thesis is organized as follows. Chapter 1 introduces the physical background of plasma–liquid discharges together with the experimental reactor configuration. Chapter 2 and 3 introduce the finite element formulation as the chosen numerical method and its implementation using the specialized *c++* library *deal.II* for Finite elements [6]. Finally, Chapter 4 presents the numerical results and their comparison with experimental observations.

Chapter 1

Physical model of the discharge

Plasma is often referred to as the fourth state of matter. Unlike solids, liquids, or neutral gases, plasma contains a large number of electrically charged particles, including free electrons and ions. In atmospheric pressure discharges, plasma is typically created when a sufficiently strong electric field accelerates free electrons in the gas. These electrons gain kinetic energy and collide with surrounding molecules, leading to excitation and ionization processes.

During ionization, an energetic electron collides with a neutral molecule and removes one of its bound electrons,

$$e^- + M \rightarrow 2e^- + M^+, \tag{1.1}$$

where M denotes a neutral molecule. The newly released electron can then ionize additional molecules, producing an avalanche multiplication process. Once the ionization rate becomes sufficiently high, a self-sustained electrical discharge is formed.

In air at atmospheric pressure, the discharge primarily develops through collisions with nitrogen and oxygen molecules. A side effect is the creation of nitrogen/oxygen radicals, whose reactive properties make them very interesting for agriculture, enviromental treatmenet and food processing.

In plasma–liquid systems, the discharge develops in direct contact with a liquid surface. Reactive species generated in the gas phase may diffuse into the liquid leading to effective nitrogen fixation [1], [3]. In this chapter, we present the experimental setup designed to study and optimize this process first presented by Hoffer et al. [4].

1.1 Reactor geometry and experimental configuration

The experimental reactor investigated in this thesis is based on the dielectric barrier discharge like configuration introduced by Hoffer et al. [4]and later studied in greater detail by Arora et al. [5]. The reactor schematic is shown in Fig. 1.1. It consists of coplanar brass electrodes placed at the bottom of a plastic chamber and separated by insulating blades. A thin flowing layer of water is maintained above the blade surface, while the discharge develops at the air–water interface.

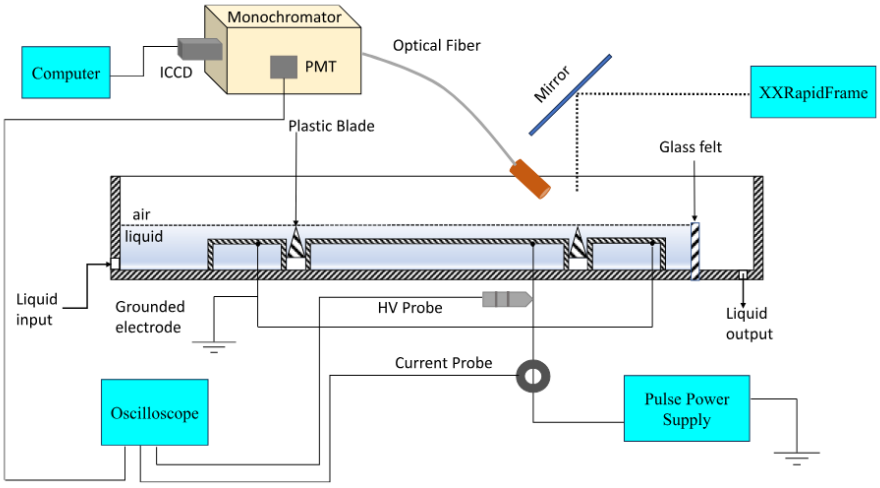


Figure 1.1: Schematic of the experimental setup of nanoseconds discharge on water-air interface taken from [5].

As discussed by Arora et al. [5], conventional plasma–liquid systems often employ metallic electrodes positioned directly above the liquid surface. In such configurations, direct interaction between the plasma and the electrode material may lead to electrode erosion and contamination of the treated liquid. The submerged electrode geometry used in this reactor was designed specifically to avoid these effects while simultaneously stabilizing the discharge position.

During operation, short high voltage pulses are applied between neighboring electrodes. The insulating blade serves as a dielectric gap and as a result, a large potential gradient develops in the vicinity of the blade tip, which also extends into the gas above the liquid surface. Once the local electric field exceeds the dielectric strength of air, gas breakdown begins to take place and a plasma discharge is formed near the blade.

Experimental observations reported by Hoffer et al. [4]demonstrated that the discharge initially develops as a diffuse bi-directional ionization wave propagating away from the blade along the air–water interface. In later stages of the discharge, there is a transition of the diffuse plasma structure into localized filamentary channels known as streamers.

1.2 Reference experimental data

The numerical results obtained in this work are compared with the experimental measurements reported by Arora et al. [5]. The experiments were performed using deionized (DI) water and tap water in the plasma–liquid reactor described previously. The measured quantities were the applied pulsed voltage, discharge current, and optical emission detected by a photomultiplier tube (PMT). This is detecting light emitted by plasma above the water surface.

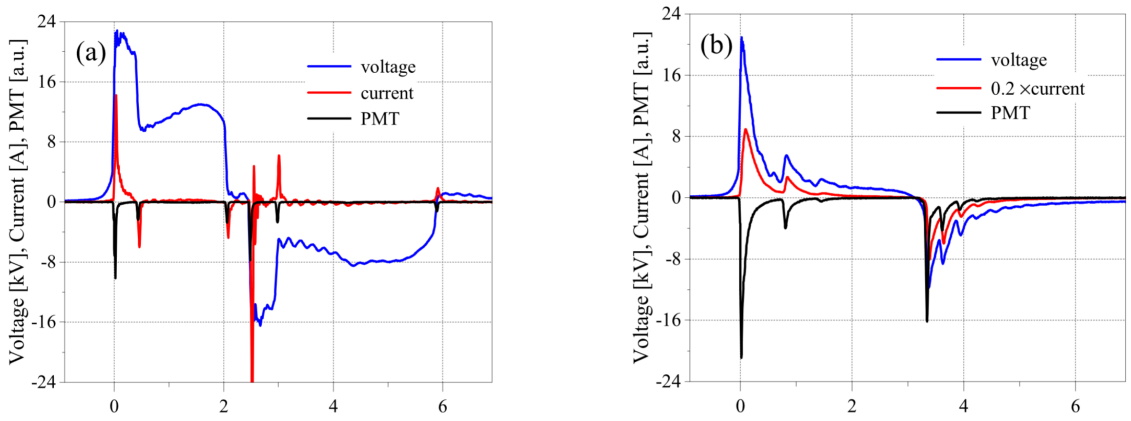


Figure 1.2: Waveforms of pulsed voltage, discharge current, and photomultiplier tube (PMT) of (a) DI (b) tap water taken from [5]

The general shape of the voltage pulse is mostly the behaviour of a high voltage power supply used for the experiment. It is bipolar, which means it provides a positive and a negative high voltage pulse in a short period.

A significant difference can be observed between the behavior of DI water and conductive tap water. In the case of tap water, the current is roughly proportional to voltage, so it behaves mostly like a resistor. The intensity of the detected light is interestingly also proportional to voltage and we observe sustained plasma filaments.

For DI water, the discharge behavior is significantly different. Plasma emission is observed mainly during periods of rapid voltage change, while during the intervals when voltage is relatively constant but still very high, almost no PMT activity is detected. The lack of discharges means, that although voltage is high, the electric field in air, isn't strong enough for gas breakdown, which means it must be shielded by some other accumulated charge. The explanation given by Hoffer et al. [4]is that surface charges accumulate on the water surface from the plasma filaments and subsequently block most of the electric field.

1.3 Physical processes relevant for numerical modelling

Although the plasma discharge itself is governed by highly complex non-equilibrium processes, the primary objective of this thesis is the numerical investigation of the electric field distribution and Joule heating inside the reactor geometry.

1.3.1 Electrostatic approximation

The complete electromagnetic behavior of the reactor is generally governed by Maxwell's equations. However, the characteristic dimensions of the reactor are significantly smaller than the electromagnetic wavelength corresponding to the applied nanosecond voltage pulses. Under these conditions, wave propagation effects and radiative phenomena can be neglected and the problem will be treated within the quasi-electrostatic approximation.

Within this approximation, the electric field is given as the gradient of the scalar electric potential

$$\mathbf{E} = -\nabla\phi. \tag{1.2}$$

The electric displacement field is related to the electric field intensity through the relation

$$\mathbf{D} = \varepsilon\mathbf{E}, \tag{1.3}$$

where ε denotes the permittivity of the material. In regions containing free electric charge density ρ, Gauss's law in terms of the displacement field $\mathbf{D}$ yields Poisson's equation

$$\nabla\cdot(\varepsilon\nabla\phi) = -\rho. \tag{1.4}$$

In charge-free regions, the governing equation reduces to Laplace's equation

$$\nabla\cdot(\varepsilon\nabla\phi) = 0. \tag{1.5}$$

The dielectric polarization of water is mainly caused by rotation of polar water molecules in response to the applied electric field. Since the molecules possess inertia and interact with neighboring molecules, their orientation cannot change instantaneously. As a result, the polarization response requires a finite amount of time.

For slowly varying electric fields, the molecules are able to follow the field almost completely and water shows a high dielectric permittivity. However, when the electric field changes rapidly, the molecular orientation begins to lag behind the applied field. The frequency dependence of the complex permittivity can be approximated using the Debye relaxation model

$$\varepsilon(\omega) = \varepsilon_\infty + \frac{\varepsilon_s - \varepsilon_\infty}{1 + i\omega\tau}, \tag{1.6}$$

where ε_s is the static permittivity, ε_∞ is the high-frequency limit of permittivity, ω is the angular frequency, and τ is the dielectric relaxation time. For water at room temperature, typical values are $\varepsilon_s \approx 80$, $\varepsilon_\infty \approx 5$, and $\tau \approx 8\,\text{ps}$. Assuming a characteristic pulse rise time of approximately $t_r \sim 50\,\text{ns}$, the dominant frequency component can be estimated as $1/t_r$. Substituting into the Debye model gives approximetly

$$\varepsilon_r \approx 79. \tag{1.7}$$

Consequently, the use of a constant dielectric permittivity in the electrostatic model is a reasonable approximation.

1.3.2 Equivalent electrical model

Once the electric field distribution is known, the conductive current density inside the liquid can be estimated using Ohm's law

$$\mathbf{J} = \sigma\mathbf{E}, \tag{1.8}$$

where σ denotes the electrical conductivity of the medium. The total conductive current flowing through a surface S is then obtained as

$$I = \int_S \mathbf{J} \cdot \mathbf{n} \, \mathrm{d}S. \tag{1.9}$$

Together with the applied voltage, we can calculate the effective resistance

$$R = \frac{U}{I}. \tag{1.10}$$

In addition to the conductive current, there is also a displacement current associated with charging of the dielectric interface. The total charge accumulated on the electrode surface can be obtained from the electric displacement field

$$Q = \int_S \mathbf{D} \cdot \mathbf{n} \, \mathrm{d}S, \tag{1.11}$$

The effective capacitance of the reactor can then be estimated from the relation

$$C = \frac{Q}{U}. \tag{1.12}$$

The displacement current is given by the time derivative of charge

$$I = \frac{\mathrm{d}Q}{\mathrm{d}t}. \tag{1.13}$$

Assuming approximately constant capacitance, this leads to the familiar relation

$$I = C\frac{\mathrm{d}U}{\mathrm{d}t}. \tag{1.14}$$

Looking at the waveforms on Fig. 1.2, we see that in the case of deoinized water the circuit behaves mostly like a capacitor and for tap water it behaves mostly like a condutor. We will therefore use a simplified circuit model as shown in Fig. 1.3. The resistive branch represents conductive current through the liquid, while the capacitive branch represents charging of the dielectric interface and accumulation of surface charge.

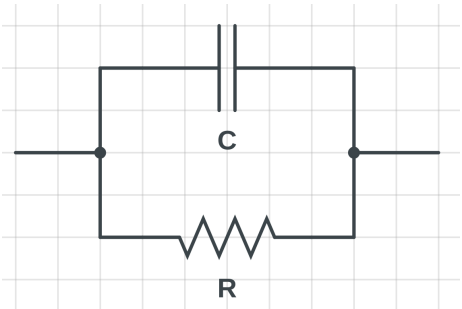


Figure 1.3: Simplified equivalent electrical model of the plasma–liquid reactor.

1.3.3 Surface charge formation

Although we would like to include the formation of surface charges present in the case of deionized water as discussed in the previous section, it doesn't seem possible to estimate what should be it's density be exactly. The expected influence of these charges on the measured current will be discussed later in the thesis.

1.3.4 Joule heating in the liquid phase

The conductive component of the discharge current leads to energy deposition inside the liquid phase in the form of Joule heating. The volumetric power density generated by conductive currents is given by

$$p = \mathbf{J} \cdot \mathbf{E}. \tag{1.15}$$

Assuming Ohm's law,

$$\mathbf{J} = \sigma \mathbf{E}, \tag{1.16}$$

the deposited power density may be expressed as

$$p = \sigma E^2. \tag{1.17}$$

Continuous operation should therefore lead to temperature increase and faster evaporation of water. Since the electrical conductivity of water depends on temperature, thermal effects may modify the electric field distribution itself. The effect is expected to be samll enough to be neglected and we will not include it in our model.

Chapter 2

Finite element method

In this chapter, we introduce the finite element method used to solve the electrostatic problem numerically. We first derive the weak formulation of the Poisson equation and then present a mixed formulation based on the electric displacement field, which provides improved conservation properties across material interfaces.

2.1 Weak formulation

The problem in question will be solving the Poisson equation for electric potential φ

$$-\nabla \cdot \varepsilon(\vec{r}) \nabla \varphi(\vec{r}) = \rho \quad \vec{r} \in \Omega \tag{2.1}$$

with Dirichlet or Neuman conditions on the boundaries

$$\begin{cases} \varphi(\vec{r}) = \varphi_0(\vec{r}), & \vec{r} \in \partial\Omega_D, \\ \hat{n} \cdot \varepsilon(\vec{r}) \nabla \varphi(\vec{r}) = g(\vec{r}), & \vec{r} \in \partial\Omega_N. \end{cases} \tag{2.2}$$

This formulation of equation (2.1) is known as the strong form. In the strong form (2.1), both the solution φ and permittivity $\varepsilon(\vec{r})$ are required to be sufficiently smooth for the derivatives to exist everywhere in the domain. In many practical situations however, such regularity cannot be guaranteed. For example, material properties such as permittivity $\varepsilon(\vec{r})$ being discontinuous across material interfaces leads to solutions whose derivatives are not defined in the classical sense. Rather than enforcing the equation pointwise, it is therefore natural to adopt the weak formulation, which relaxes the differentiability requirements and allows piecewise smooth solutions. To begin, we multiply the strong form (2.1) by a test function $v(\vec{r})$ and integrate over the domain Ω.

$$-\int_\Omega v \nabla \cdot (\varepsilon \nabla \varphi)\, d\Omega = \int_\Omega v \rho \, d\Omega. \tag{2.3}$$

Applying the divergence theorem to the left hand side gives

$$-\int_\Omega v \nabla \cdot (\varepsilon \nabla \varphi)\, d\Omega = -\int_{\partial\Omega} v\, (\varepsilon \nabla \varphi \cdot \hat{n})\, d\Gamma + \int_\Omega \varepsilon \nabla v \cdot \nabla \varphi \, d\Omega. \tag{2.4}$$

We now restrict the test functions $v(\vec{r})$ to those which vanish on the Dirichlet boundary $\partial\Omega_D$. This reflects the fact that the solution is fixed there and cannot be varied.

$$\int_{\partial\Omega} v\,(\varepsilon\nabla\varphi\cdot\hat{n})\,d\Gamma = \int_{\partial\Omega_N} v\,g\,d\Gamma. \tag{2.5}$$

Substituting this into (2.3), the weak formulation reads:

$$\int_{\Omega} \varepsilon\nabla v\cdot\nabla\varphi\,d\Omega = \int_{\Omega} v\,\rho\,d\Omega + \int_{\partial\Omega_N} v\,g\,d\Gamma \tag{2.6}$$

Here, the gradient operator is also understood only weakly. We say that a function $\varphi\in L^2(\Omega)$ has a weak gradient $\nabla\varphi\in[L^2(\Omega)]^d$ if for all smooth test functions $w\in C_c^\infty(\Omega)^d$ it holds that

$$\int_{\Omega} \varphi\,\nabla\cdot w\,d\Omega = -\int_{\Omega}(\nabla\varphi)\cdot w\,d\Omega. \tag{2.7}$$

This motivates choosing the solution and test functions from the Sobolev space $H^1(\Omega)$, defined as

$$H^1(\Omega) = \{u\in L^2(\Omega)\,|\,\nabla u\in[L^2(\Omega)]^d\},$$

each with their respective constraints

$$V_\varphi = \{\varphi\in H^1(\Omega)\,|\,\varphi|_{\partial\Omega_D}=\varphi_0\},\quad V=\{v\in H^1(\Omega)\,|\,v|_{\partial\Omega_D}=0\}.$$

The weak formulation then consists of finding $\varphi\in V_\varphi$ such that (2.6) holds for all $v\in V$.

2.2 Finite element discretization

The weak formulation derived in the previous section is posed over infinite-dimensional function spaces. In order to solve it numerically, the finite element method proceeds by restricting the problem to finite-dimensional subspaces.

Let $V_h\subset V$ and $V_{\varphi,h}\subset V_\varphi$ be finite-dimensional subspaces spanned by a set of basis functions $\{\phi_i(\vec{r})\}_{i=1}^N$. The approximate solution φ_h is then expressed as a linear combination of these basis functions:

$$\varphi_h(\vec{r}) = \sum_{j=1}^{N} u_j\,\phi_j(\vec{r}), \tag{2.8}$$

where u_j are unknown coefficients to be determined. Choosing the test functions v_h to be the same set of basis functions ϕ_i than leads to a system of linear equations

$$\sum_{j=1}^{N} u_j \int_{\Omega} \varepsilon\nabla\phi_i\cdot\nabla\phi_j\,d\Omega = \int_{\Omega}\phi_i\,\rho\,d\Omega + \int_{\partial\Omega_N}\phi_i\,g\,d\Gamma. \tag{2.9}$$

Written in matrix form we have

$$\mathbf{Ku} = \mathbf{f}, \tag{2.10}$$

where the stiffness matrix $\mathbf{K}$ and right hand side vector $\mathbf{f}$ are defined by

$$K_{ij} = \int_\Omega \varepsilon \nabla \phi_i \cdot \nabla \phi_j \, d\Omega, \quad f_i = \int_\Omega \phi_i \rho \, d\Omega + \int_{\partial\Omega_N} \phi_i g \, d\Gamma.$$

The choice of basis functions ϕ_i is determined by a discretization of the domain Ω into smaller subdomains, or elements. Typically, these basis functions are taken to be piecewise polynomial functions that are nonzero only on a small number of elements, leading to a sparse system matrix $\mathbf{K}$.

2.3 Mixed formulation

In the previous chapter, the problem was formulated in terms of the electric potential φ, with the electric field given by $\vec{E} = -\nabla\varphi$. While this approach is convenient, it has a few limitations. Standard finite element approximations based on $H^1(\Omega)$ enforce no continuity of $\nabla\varphi$ across elements or material interfaces, which can lead to undesirable and non physical results. To address this, we reformulate the problem by introducing the electric displacement field as an independent variable.

$$\vec{D} = -\varepsilon \nabla \varphi \tag{2.11}$$

This allows us to rewrite the Poisson equation (2.1) as a system of first-order equations

$$\varepsilon^{-1}\vec{D} + \nabla\varphi = 0, \tag{2.12}$$

$$\nabla \cdot \vec{D} = \rho, \tag{2.13}$$

where boundary conditions become

$$\begin{cases} \varphi(\vec{r}) = \varphi_0(\vec{r}), & \vec{r} \in \partial\Omega_D \\ \hat{n} \cdot \vec{D} = g(\vec{r}), & \vec{r} \in \partial\Omega_N. \end{cases} \tag{2.14}$$

In a similar spirit as before, we will multiply (2.12) by a vector valued test function $\vec{v}$ and (2.13) by a scalar w and integrate over the domain.

$$\int_\Omega \vec{v} \cdot \varepsilon^{-1}\vec{D} \, d\Omega + \int_\Omega \vec{v} \cdot \nabla\varphi \, d\Omega = 0 \tag{2.15}$$

$$\int_\Omega w \nabla \cdot \vec{D} \, d\Omega = \int_\Omega w \rho \, d\Omega \tag{2.16}$$

Integrating the second term of equation (2.15) by parts and plugging in for the boundary conditions we obtain

$$\int_\Omega \vec{v} \cdot \nabla\varphi \, d\Omega = -\int_\Omega \varphi \nabla \cdot \vec{v} \, d\Omega + \int_{\partial\Omega_D} \varphi_0 \vec{v} \cdot \hat{n} \, d\Gamma + \int_{\partial\Omega_N} \varphi g \, d\Gamma \tag{2.17}$$

where we will require, that the test functions $\vec{v}$ satisfy $\vec{v} \cdot \hat{n} = 0$ on $\partial\Omega_N$, so that the last term drops out. Substituting into (2.15) grants us the weak formulation

$$\int_\Omega \vec{v}\cdot\varepsilon^{-1}\vec{D}\,d\Omega - \int_\Omega \varphi\nabla\cdot\vec{v}\,d\Omega = -\int_{\partial\Omega_D}\varphi_0\vec{v}\cdot\hat{n}\,d\Gamma \quad \forall\vec{v}, \tag{2.18}$$

$$-\int_\Omega w\nabla\cdot\vec{D}\,d\Omega = -\int_\Omega w\rho\,d\Omega \quad \forall w. \tag{2.19}$$

Note that in this form, Dirichlet boundary conditions are incorporated weakly. Therefore, it is not necessary to enforce them strongly and we can look for the potential ϕ in the most general space $L^2(\Omega)$ as it's also not differentiated anywhere in the formulas. The test functions w also have no restrictions, since they do not appear in any of the boundary integrals. What we need to enforce strongly on the other hand are the Neuman boundary conditions for $\vec{D}$ and zero normal components for the $\vec{v}$ test functions. With these considerations, the solution and test function spaces are

$$W_\varphi = \{\varphi \in L^2(\Omega)\}, \qquad V_D = \{\vec{D} \in H(\mathrm{div};\Omega) \quad \vec{D}|_{\partial\Omega_N} = g\},$$
$$W = \{w \in L^2(\Omega)\}, \qquad V = \{\vec{v} \in H_0(\mathrm{div};\Omega) \quad \vec{v}|_{\partial\Omega_N} = 0\}.$$

The choice of the discrete subspaces $V_h \subset V$ and $W_h \subset W$ is not arbitrary. As detailed in Boffi, Brezzi, and Fortin [7], mixed formulations of this type fall into the class of saddle point problems. A well known requirement for the stability and convergence of such problems is the Ladyzhenskaya Babuška Brezzi (LBB) or inf sup condition. If the spaces for the vector field $\vec{D}$ and the scalar potential φ are chosen inappropriately, the resulting system may become unstable, often manifesting as spurious oscillations in the solution.

To ensure stability, we use Raviart Thomas (RT_k) finite element spaces for the electric displacement $\vec{D}$ together with discontinuous polynomial spaces (DG_k) for the potential φ. This pair is known to satisfy the discrete inf-sup condition. An important additional advantage of Raviart Thomas elements is that they are div-conforming, meaning that the normal component of the displacement field remains continuous across element interfaces. As a result, local conservation laws are automatically preserved by the discretization. Similar formulations are commonly used in fluid dynamics and transport problems, where exact local conservation of mass or flow is important. This constraint would not be possible to enforce strongly using the first formulation.

2.4 Convergence and Error Estimation

The reliability of the mixed finite element method developed in the previous chapter depends on its stability and convergence properties. This chapter develops a priori error estimates that predict expected convergence rates under uniform refinement, and computable a posteriori error estimators necessary for adaptive mesh refinement.

2.4.1 A Priori Error Estimates

To quantify the accuracy of the mixed finite element approximation, we consider a sequence of triangulations $\mathcal{T}_h$ of the domain Ω. We define the mesh size parameter h as the maximum diameter of the elements K in the triangulation:

$$h = \max_{K \in \mathscr{T}_h} (\operatorname{diam} K). \tag{2.20}$$

The process of uniform refinement refers to a systematic reduction of h where each element is subdivided into smaller entities of the same geometric type (e.g., quadrilateral into four smaller quads). As the size of our elements shrinks and we compute on finer meshes $\mathscr{T}_h$, we expect the solutions $\vec{D}_h$ and φ_h to approach the exact solutions $\vec{D}$ and φ. The expected convergence rates is the subject of a priori error estimates. An important condition for these to hold, is that the refinement must be shape-regular, meaning the elements do not become excessively thin or stretched as $h \to 0$.

In the following text, the notation $\|\cdot\|$ denotes the $L^2(\Omega)$-norm. For a scalar function φ, this is defined as:

$$\|\varphi\| = \left(\int_\Omega |\varphi|^2 \, d\Omega \right)^{1/2}, \tag{2.21}$$

and similarly for the vector field $\|\vec{D}\|$. We will also introduce the Sobolev semi-norms of order k, which measure the L^2 norm of the k-th order derivatives.

$$\|\varphi\|_{H^k} = \left(\sum_{|\alpha|=k} \|D^\alpha \varphi\|_{L^2}^2 \right)^{1/2} \tag{2.22}$$

In this formula α denotes a multi-index $\alpha = (\alpha_1, \ldots, \alpha_d)$, with the norm $|\alpha| = \sum \alpha_i$ and D^α are the corresponding derivatives.

$$D^\alpha \varphi = \frac{\partial^{|\alpha|} \varphi}{\partial x_1^{\alpha_1} \ldots \partial x_d^{\alpha_d}} \tag{2.23}$$

For vectors, we analogously define

$$\|\vec{D}\|_{H^k} = \left(\sum_{i=1}^{d} \|D_i\|_{H^k}^2 \right)^{1/2}. \tag{2.24}$$

Following the analysis in Boffi, Brezzi, and Fortin [7], for the Raviart-Thomas spaces (RT_k) of order k paired with discontinuous polynomials (DG_k) of order k, the following a priori error estimates hold.

$$\|\vec{D} - \vec{D}_h\| \leq C h^{k+1} \|\vec{D}\|_{H^{k+1}} \tag{2.25}$$

$$\|\nabla \cdot (\vec{D} - \vec{D}_h)\| \leq C h^{k+1} \|\nabla \cdot \vec{D}\|_{H^{k+1}} \tag{2.26}$$

$$\|\varphi - \varphi_h\| \leq C h^{k+1} \|\varphi\|_{H^{k+1}} \tag{2.27}$$

The constant C appearing in these estimates is independent of the mesh size h. In particular, the bounds predict that the numerical error decreases proportionally to h^{k+1} under uniform refinement. The constant C may depend on the shape regularity of the mesh and the geometry of the domain, but not on the refinement level itself.

The Sobolev norms on the right-hand side measure the regularity of the exact solution. Smooth solutions with bounded higher order derivatives therefore lead to smaller approximation errors. On the other hand, if the exact solution contains sharp gradients or singular behavior, the convergence rates may deteriorate because the required Sobolev regularity assumptions are no longer satisfied.

2.4.2 A Posteriori Error Estimation

While a priori estimates provide theoretical guarantees for convergence rates, they can't be computed without the unknown exact solution. There is however a way to estimate it, which is the role of a posteriori error estimate. In practical applications, it is essential to have a computable bound to monitor the actual error and possibly also drive adaptive mesh refinement.

Following the work of Carstensen [8], we introduce a posteriori error estimator η_h for the mixed finite element method. For each element T in the triangulation $\mathscr{T}_h$, we define the local error indicator η_T as:

$$\begin{aligned}\eta_T^2 =& \|\rho - \nabla\cdot\vec{D}_h\|_{L^2(T)}^2 + h_T^2\|\nabla\times(\varepsilon^{-1}\vec{D}_h)\|_{L^2(T)}^2 \\ &+ h_T^2\|\varepsilon^{-1}\vec{D}_h + \nabla\phi_h\|_{L^2(T)}^2 + \|h_E^{1/2}J(\varepsilon^{-1}\vec{D}_h\cdot\vec{t})\|_{L^2(\partial T)}^2\end{aligned} \tag{2.28}$$

where h_T is the element diameter, h_E is the edge length, and $J(\cdot)$ denotes the jump of the tangential component across the element boundary. The global estimator is defined as the sum of all element contributions:

$$\eta_h := \left(\sum_{T\in\mathscr{T}_h}\eta_T^2\right)^{1/2} \tag{2.29}$$

According to Theorem 2.1 in Carstensen [8], for Raviart-Thomas, Brezzi-Douglas-Marini, or Brezzi-Douglas-Fortin-Marini elements, there exists a positive constant C_1 such that the total error is bounded from above:

$$e = \left(\|\vec{D}-\vec{D}_h\|^2 + \|\nabla\cdot(\vec{D}-\vec{D}_h)\|^2 + \|\varphi-\varphi_h\|^2\right)^{\frac{1}{2}} \le C_1\eta_h. \tag{2.30}$$

Furthermore, under the assumption that the material parameters and discrete solutions are locally polynomial, the estimator is efficient, meaning it also provides a lower bound on the error:

$$C_2\eta_h \le e. \tag{2.31}$$

This dual property ensures that η_h is a reliable indicator for adaptive refinement algorithms, allowing for the concentration of computational resources in regions where the error is highest.

Chapter 3

Implementation

3.1 Geometry and Meshing

The first step in constructing a numerical model is modeling the geometry of the experimental setup. The physical dimensions of the reactor were obtained from direct measurements. These measurements are illustrated in Fig. 3.1 and Fig. 3.2, which show the side and top views of the apparatus, respectively.

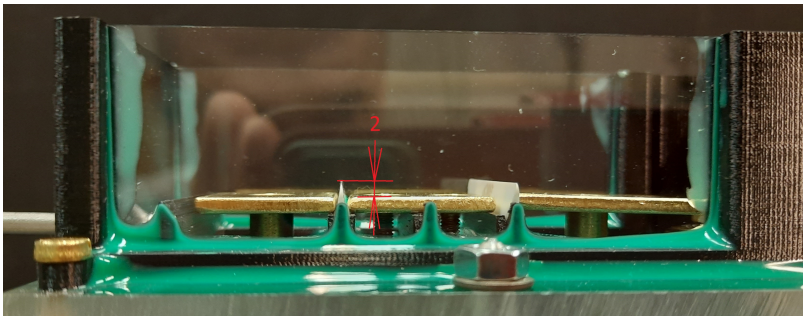


Figure 3.1: Side view of the experimental setup with indicated characteristic dimensions used for geometric reconstruction.

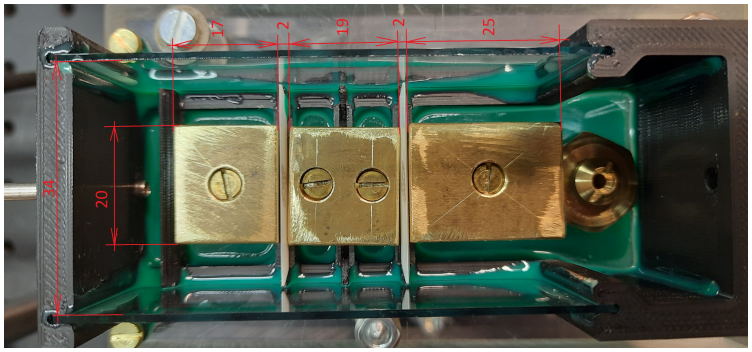


Figure 3.2: Top view of the experimental setup showing the electrode arrangement and blade spacing.

To reduce computational cost, the full three-dimensional geometry was simplified to a two-dimensional model corresponding to the side view of the reactor. This approximation assumes translational invariance in the out of plane direction.

The experimental electrode arrangement consists of three electrodes in a $(- + -)$ configuration, separated by two insulating blades. Rather than modeling the full geometry, the problem is reformulated in terms of a periodically repeating unit in the horizontal direction. As a result, the computational domain contains halves of two neighboring electrodes and a single blade between them.

Based on the measured dimensions, a geometric outline of the reactor was constructed, as shown in Fig. 3.3. A critical feature of the geometry is the sharp blade tip, which has a characteristic radius of approximately $7\,\mu$m. The tip is modeled as a circular arc inscribed into the blade angle. This construction is illustrated in Fig. 3.4.

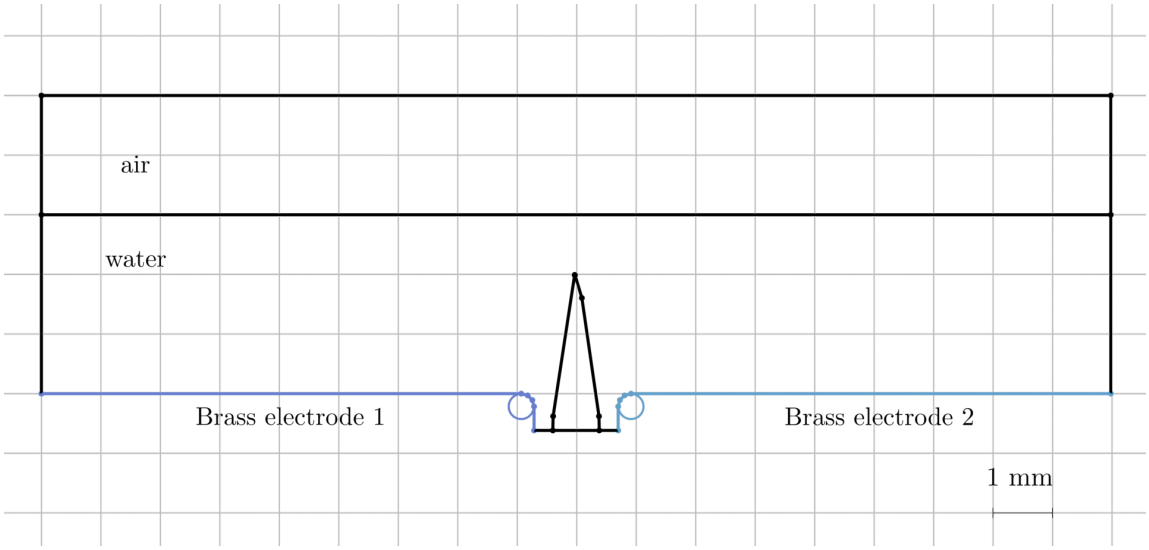


Figure 3.3: Reconstructed geometric outline of the computational domain derived from experimental measurements.

The reduced domain is interpreted as a periodically repeating unit in the horizontal direction which allows us to assign Neuman boundary conditions on the walls. (Disregarding the slightly asymmetic blade). For simplicity, all outer boundaries are, also assigned homogeneous Neumann boundary conditions

$$\frac{\partial \phi}{\partial n} = 0. \tag{3.1}$$

The electrodes themselves are equipotential surfaces assigned with Dirichlet boundary conditions.

The next step is to discretize the computational domain. The geometry must be divided into a finite number of smaller subdomains called elements. This process is referred to as meshing. The finite element method then constructs the discrete approximation of the solution using basis functions defined locally on these elements. The quality and resolution of the mesh therefore strongly influence the accuracy of the numerical solution.

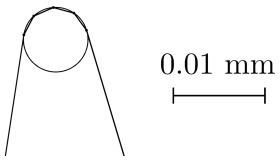


Figure 3.4: Detailed representation of the blade tip geometry. The sharp edge is approximated by a circular arc with a radius of $7\,\mu$m.

Mesh generation presents a significant challenge due to the multiscale nature of the problem. In the vicinity of the blade tip we require element sizes on the order of a few micrometers. At the same time, the overall domain extends to millimeter scales, which would make uniformly fine mesh very computationally expensive.

Standard automatic meshing tools were considered but found unsuitable for this application. The primary issue is their inability to robustly handle the extreme variation in spatial scales. Equally problematic is that we prefer the discretization to be performed using quadrilateral elements. This choice is motivated by their favorable properties in representing gradients in the Finite element method and the numerical framework *deal.II* is also optimized for quadrilateral meshes for this reason. However, most automatic meshing tools primarily generate triangular meshes.

To address these constraints, the mesh was constructed manually. The process begins with a high-resolution discretization of the blade tip region. From this region, the mesh was expanded outward in a structured manner resembling a radial or "spider-web" pattern. This allows for a gradual increase in element size, reaching approximately 0.1 mm near the outer boundaries while maintaining fine resolution near the tip.

The resulting mesh is shown in Fig. 3.7, with detailed views of the tip region provided in Fig. 3.5 and Fig. 3.6.

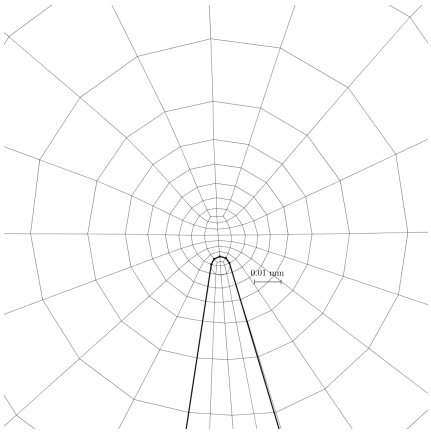


Figure 3.5: Close-up of the mesh near the blade tip showing the high-resolution discretization.

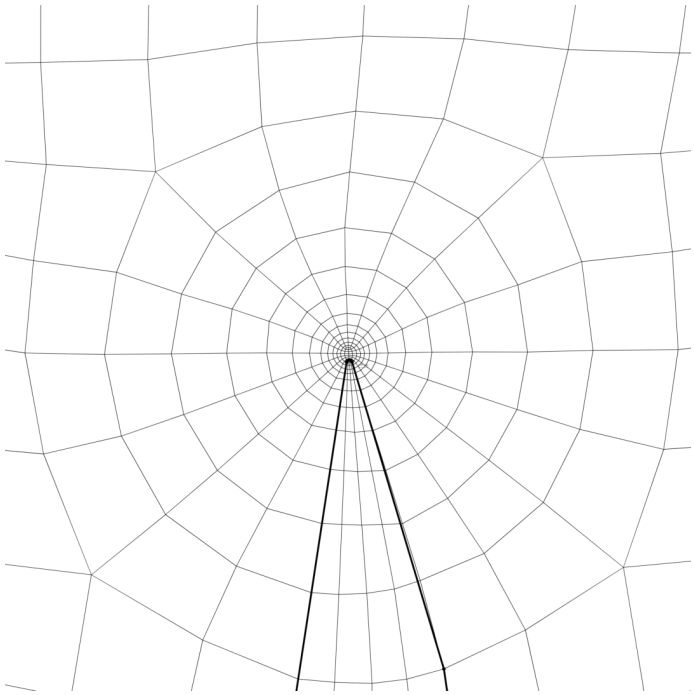


Figure 3.6: Intermediate view of the mesh demonstrating the transition from fine to coarse elements.

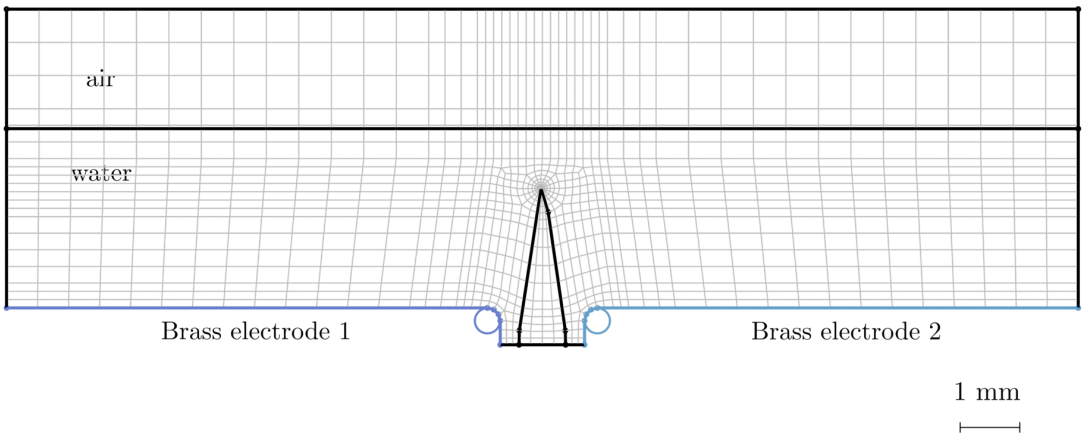


Figure 3.7: The final computational mesh.

3.2 Test case for the numerical method

Before applying the method to the created geometry, we will validate the implementation on a problem with a known analytical solution. The goal is to verify that the discretisation achieves the expected convergence rates for both the primary variables and the error estimators introduced in the previous chapter.

3.2.1 Test case definition

To effectively test our implementation, we employ the method of manufactured solutions. We prescribe a sufficiently smooth electric potential ϕ and permittivity ε and then compute the corresponding source term ρ from the Poisson equation (2.1), ensuring that the triple $(\varphi, \varepsilon, \rho)$ satisfies the equation exactly everywhere in the space. The manufactured solution can be chosen at random, except that it shouldn't be representable exactly by the discretized solution space. That is we should exclude polynoms and linear functions. Choosing

$$\begin{aligned} \phi &= \sinh x \cos y \\ \varepsilon &= 1 + kx \end{aligned}$$

where, the parameter k controls the spatial variation of the material coefficient we find the displacement vector $\vec{D}$ and charge distribution ρ as

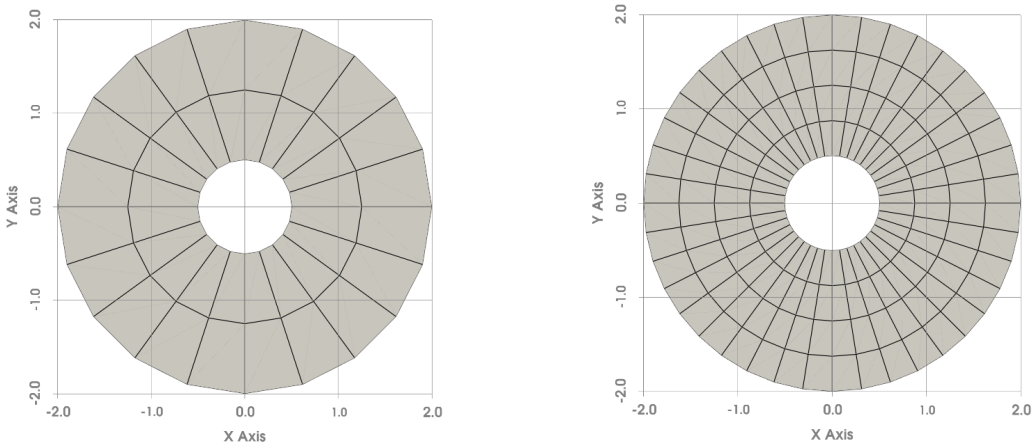
$$\begin{aligned} \vec{D} &= -\varepsilon \nabla \phi = -\varepsilon \begin{bmatrix} \cosh x \cos y \\ -\sinh x \sin y \end{bmatrix} \\ \rho &= \nabla \cdot D = -k \cosh x \cos y. \end{aligned}$$

The next thing that needs to be decided is the computational mesh. To test on something reminiscent of the created model, we consider a torus-shaped computational domain as illustrated in Fig. 3.8 a). This introduces geometric curvature and non-uniform element sizes under refinement. On this geometry we also conveniently get two separate boundaries. One will be assigned Dirichlet boundary conditions for ϕ and the second Neuman for $\vec{D}$ according to the exact solution.

$$\begin{cases} \varphi(\vec{r}) = \varphi_0(\vec{r}), & \vec{r} \in \partial\Omega_D \\ \hat{n} \cdot \vec{D} = g(\vec{r}), & \vec{r} \in \partial\Omega_N \end{cases} \tag{3.2}$$

To study convergence and test the error estimates (2.28) and (2.30) we need to iteratively solve on geometries subdivided into smaller and smaller elements so that the smallest cell parameter h decreases. The simplest approach is applying uniform refinement where each quadrilateral is subdivided into four smaller elements. On a flat geometry, we would place these newly created vertices to evenly split the cell into quarters. In our case the geometry is curved however and the newly created vertices must be placed explicitly to conform to the underlying torus. In particular, vertices located on the boundary are projected onto the exact geometric surface, ensuring that the refined mesh remains a consistent approximation of the torus. This process is illustrated on Fig. 3.8 b).

This procedure preserves the overall shape of the domain while progressively improving its geometric resolution. After n refinement steps, the mesh size decreases as $h \propto 2^{-n}$, where h is defined as the diameter of the largest element.



(a) Initial mesh before refinement.

(b) Mesh after uniform refinement.

Figure 3.8: Comparison of the computational mesh before and after uniform refinement. The refinement preserves the overall geometry while increasing resolution uniformly across the domain.

3.2.2 Test case convergence study

We now investigate the numerical convergence of the mixed finite element scheme. The mesh is uniformly refined, and errors are evaluated with respect to the exact solution. We consider different polynomial orders for the Raviart–Thomas / discontinuous Galerkin discretisation.

For each refinement level, we compute the exact errors in $\vec{D}_h$ and φ_h according to (2.30), together with the corresponding a posteriori estimator defined in (2.28). Based on the a priori analysis, the expected convergence rates are of order $\mathcal{O}(h^{k+1})$.

The numerical results confirm the theoretical predictions. For all tested polynomial orders, the convergence rates closely match the expected h^{k+1} behavior. Moreover, the a posteriori estimator tracks the true error with comparable accuracy, demonstrating both reliability and efficiency of the estimator.

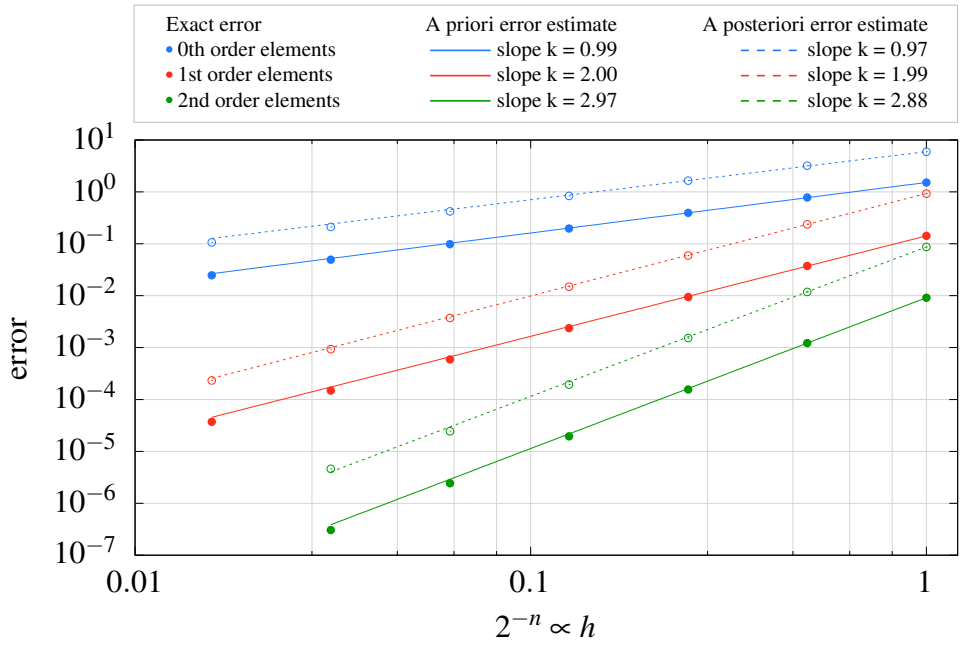


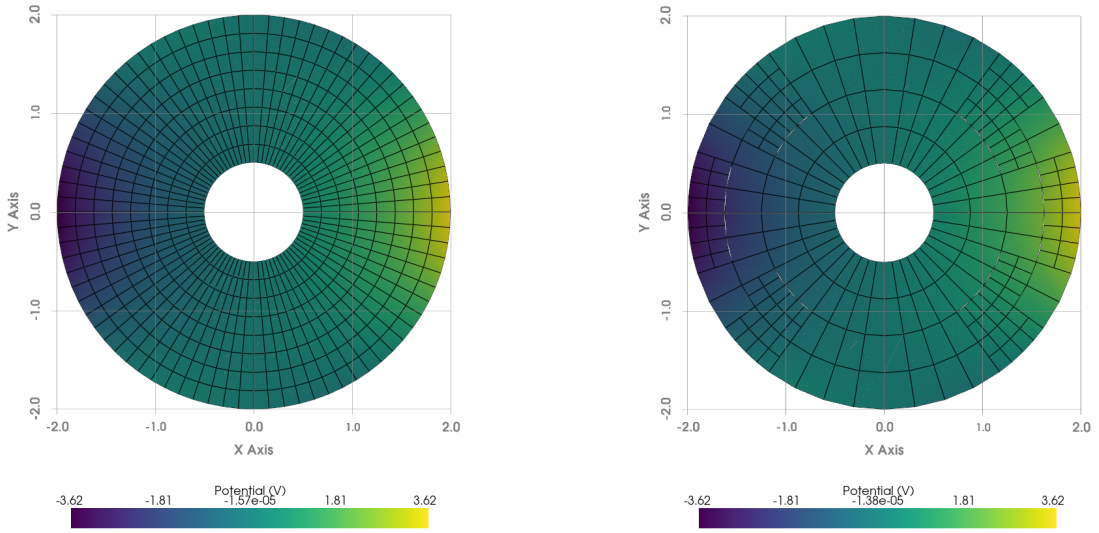
Figure 3.9: Convergence of the mixed finite element scheme for increasing polynomial order. Solid lines represent exact errors, dashed lines represent a posteriori estimates.

3.2.3 Adaptive refinement

In addition to uniform refinement, we investigate an adaptive refinement strategy driven by the a posteriori error estimator. The goal is to concentrate computational effort in regions where the local error is largest and improving efficiency compared to uniform mesh refinement.

Starting from the same initial triangulation, the adaptive procedure is applied iteratively. At each refinement step, the local error indicators η_T are evaluated according to (2.28) for all elements $T \in \mathscr{T}_h$. The elements are then sorted according to their contribution to the total error, and a subset of elements with the largest indicators is selected for refinement. In this work, we use a fixed marking strategy in which one half of the elements with the highest error indicators are refined at each step.

Refinement is performed using the same subdivision strategy as in the uniform case, ensuring consistency of the discretisation while allowing for strong local variation in mesh resolution. As a result, the mesh becomes progressively refined in regions where the solution exhibits larger local errors, while remaining coarse elsewhere.



(a) Potential solution on twice uniformly refined mesh

(b) Potential solution on twice adaptively refineed mesh

Figure 3.10: Comparison of the computed potential ϕ_h under uniform and adaptive mesh refinement.

A key complication of local refinement is the appearance of so-called hanging nodes, i.e. vertices that lie on the edge of a neighbouring element without being shared by all adjacent elements. These introduce non-conforming interfaces in the mesh and require special treatment to maintain consistency of the discrete function spaces. In particular, additional constraints must be imposed to ensure continuity properties appropriate to the chosen finite element spaces, or alternatively, the refinement must be propagated to neighbouring elements. The handling of hanging nodes is a complicated aspect of adaptive mesh refinement. In our implementation, this is handled automatically by the `deal.II` library.

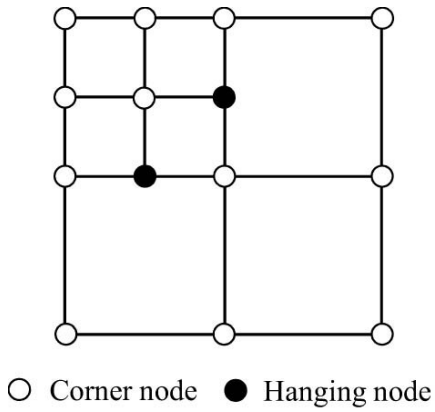


Figure 3.11: Hanging nodes introduced into triangulation by adaptive refinement.

The convergence behaviour under adaptive refinement is shown in Fig. 3.12. In contrast to uniform refinement, the convergence rates are no longer directly comparable to the theoretical $\mathcal{O}(h^{k+1})$ estimates, since the mesh size h is not reduced uniformly across the domain. Instead, the error is plotted against the diameter of the smallest cell which is also in this case proportional to 2^{-n}, where n is the number of refinement steps.

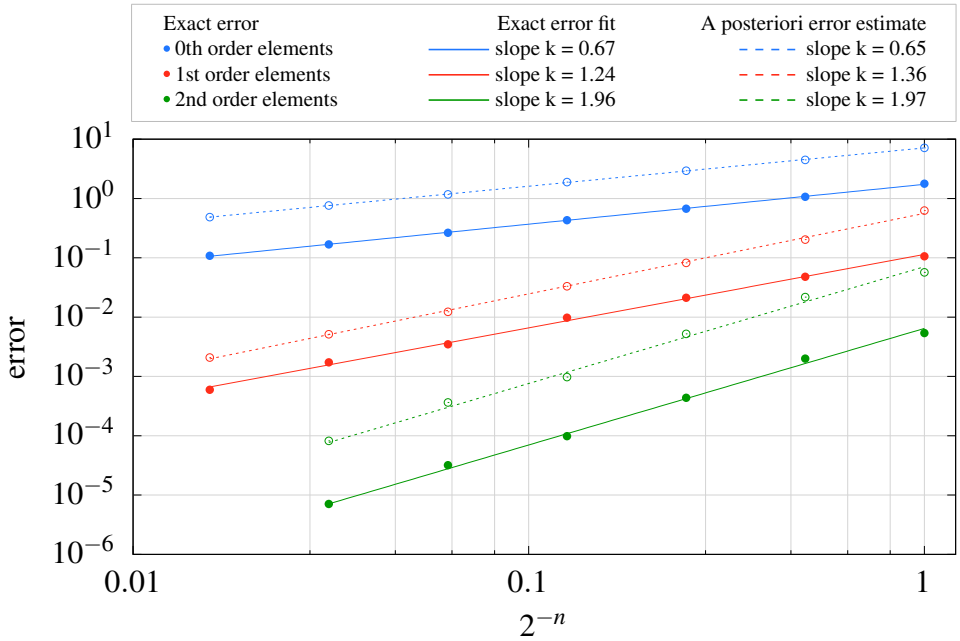


Figure 3.12: Convergence under adaptive mesh refinement. Errors are plotted against the diameter of the smallest cell. Solid lines denote exact errors, while dashed lines represent the a posteriori estimator.

The results demonstrate that adaptive refinement effectively captures regions of higher error and allocates resolution accordingly. Furthermore, the a posteriori estimator continues to track the true error closely, confirming its suitability as a refinement indicator.

Chapter 4

Computation and Results

With the numerical method validated and having modeled the reactor geometry, we proceed to compute the electric potential and displacement field within the reactor. Based on the proposed model we will calculate the expected current density and try to estimate the heating caused by this current.

4.1 Physical Parameters and Boundary Conditions

The computation was done using a normalized potential difference of 1V between the electrodes. Due to the linearity of the Poisson equation (2.1), the results obtained here can be scaled linearly to represent any experimental conditions.

The approximate material properties were assigned based on the components of the reactor. The relative permittivity values used in the model are summarized in Table 4.1.

Table 4.1: Material properties used in the simulation.

Material	Relative Permittivity ε_r
Air	1.
Water	78.
Plastic Insulator (Blade)	2.

As already discussed, the relative permittivity of dielectrics depends on the frequency of the electric field and also on temperature. Both of these efects are found to be relatively small, and we therefore assume them to be constant.

The electrodes were assigned Dirichlet boundary conditions based on the voltage difference and the remaining outer boundaries were assigned homogeneous Neumann conditions, assuming a periodically repeating unit as described in Section 4.1.

4.1.1 Numerical results and comparison with measurement

The resulting potential distribution φ and the magnitude of the electric field E calculated from the displacement field $\vec{D}$ are shown in varying levels of detail on Fig. 4.1, Fig. 4.2 and Fig. 4.3. As expected, the electric field is highly concentrated at the sharp tip of the

blade reaching around 5.32 V/mm at it's peak inside the blade. The intensity drops out very quickly and above water surface we reach just about 0.22 V/mm as can be seen on Fig. 4.4.

As a first validation step, we estimate the voltage at which electrical breakdown of the gas phase should begin above the blade. Under atmospheric conditions, the dielectric strength of air is known to be on the order of $3\,\mathrm{kV/mm}$, although the exact breakdown field depends on humidity and pressure. In our experiment, the discharge develops directly at the air–water interface. The physics occuring on this interface are the subject of further study on this experiment, but we will assume the cited number is approximately correct.

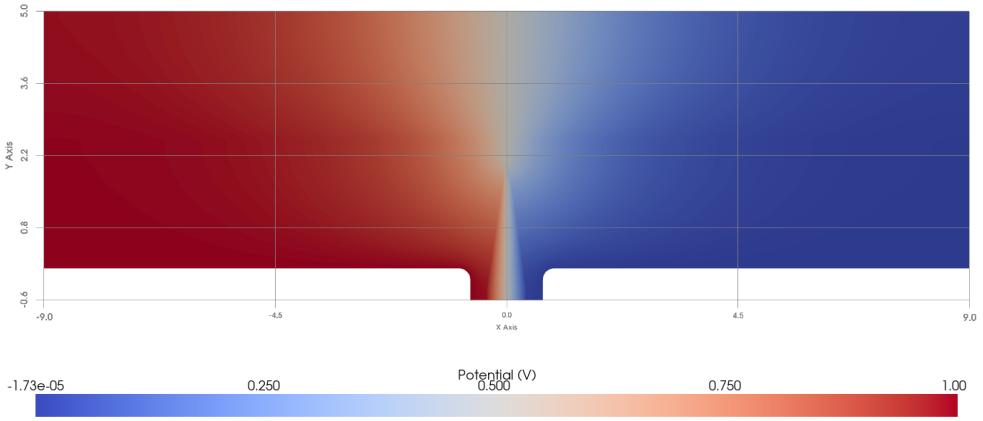


Figure 4.1: Numerical solution of the electric potential

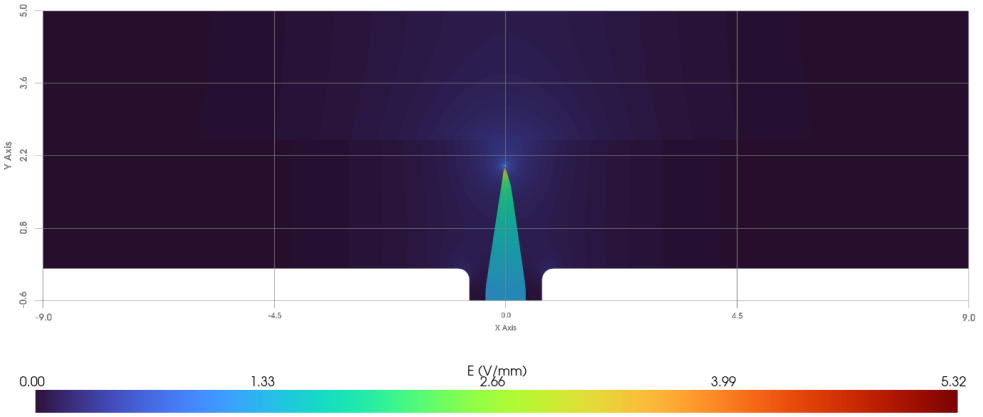


Figure 4.2: Numerical solution of the electric field $\vec{E}$ calculated from the displacement field as $\varepsilon^{-1}\vec{D}$.

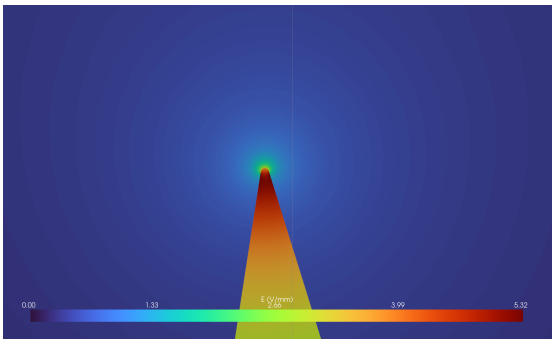


Figure 4.3: Intensity of the electric field around the blade.

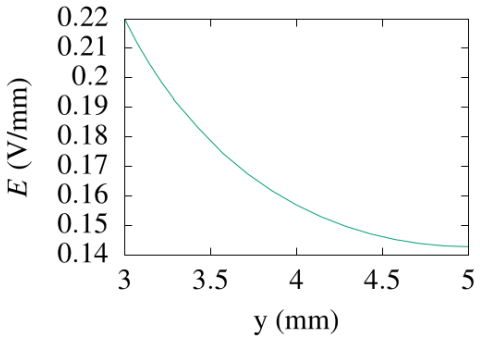


Figure 4.4: Intensity of the electric field in air above the blade. The water level is located at $y = 3\,\mathrm{mm}$.

The numerical solution predicts an electric field intensity of approximately $E \approx 0.22\,\mathrm{V/mm}$ above the water surface for an applied voltage of $U = 1\,\mathrm{V}$ as can be seen on Fig. 4.4. The breakdown is therefore expected around

$$U \approx \frac{3 \times 10^3}{0.22} \approx 13.6\,\mathrm{kV}.$$

The true operating voltage can be deduced from the experimental measurements reported in Arora et al. [5]. From Fig. 4.5 we can see that PMT spikes up for the first time at around t=-0.2 μs for both the tap and DI water, indicating, that that's when discharge begins to happen. At this time, the measured voltage between the electrodes was found to be around 8 kV. The is in a relatively good agreement considering the approximations we used.

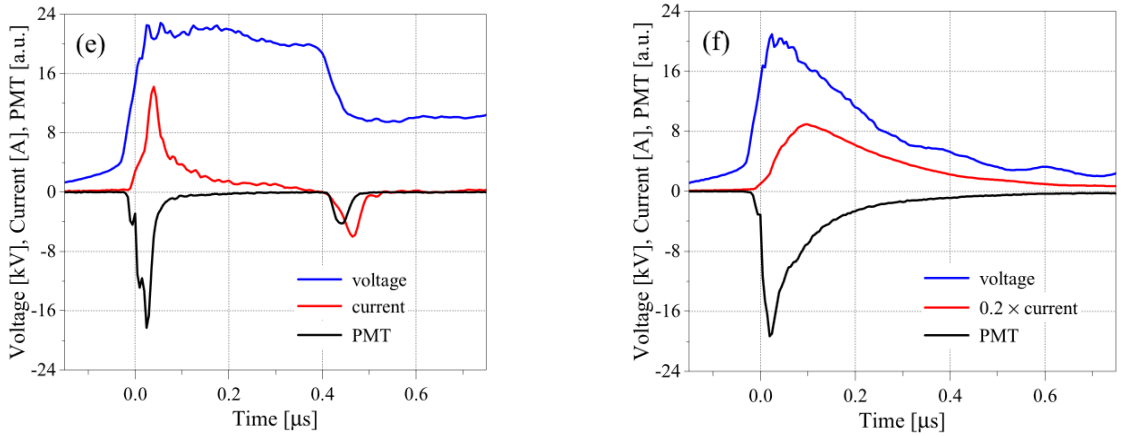


Figure 4.5: Waveforms of pulsed voltage, discharge current, and photomultiplier tube (PMT) up to the main HV pulse (e) DI (f) tap water taken from [5]

4.1.2 Equivalent circuit parameters

Having calculated the electrical field, we proceed to calculate the expected resistance and capactiance of the circuit. Since the numerical model is two-dimensional, the computed fluxes correspond to quantities per unit depth in the out-of-plane direction. The total conductive current is therefore obtained by multiplying the line integral by the reactor depth $d = 34\,\text{mm}$

$$I = 2d \int_{\Gamma} \sigma \vec{E} \cdot \hat{n}\, dl. \tag{4.1}$$

where σ is the electrical conductivity. Because the simulated geometry represents only one half of the repeating electrode structure, the resulting current is multiplied by a factor of two. The effective resistance of the reactor is then estimated from $R = U/I$. The reactor capacitance is calculated from the electric displacement flux through the electrode boundary

$$C = \frac{4d}{U} \int_{\partial\Omega_e} \vec{D} \cdot \hat{n}\, dl, \tag{4.2}$$

where an approximate factor of four accounts for the quarter-electrode symmetry used in the numerical model. Since the reactor geometry is identical for both liquids, the resulting capacitance is the same for deionized and tap water. The main difference appears in the conductive branch of the equivalent circuit. Using the experimental conductivities reported by Arora et al. [5], approximately $\sigma_{\text{DI}} \approx 1.2\,\mu\text{S}\,\text{cm}^{-1}$ and $\sigma_{\text{tap}} \approx 450\,\mu\text{S}\,\text{cm}^{-1}$, the estimated RC circuit parameters are summarized in Table 4.2.

Water type	Resistance R	Capacitance C
DI water	0.50 MΩ	17 pF
Tap water	1.3 kΩ	17 pF

Table 4.2: Estimated equivalent circuit parameters of the reactor.

To compare the numerical model with the measurements, the measured current waveforms were fitted using the RC circuit model. The results are shown in Figures 4.7 and 4.6. For deionized water, the measured current was mostly the capacitive component, while the resistive contribution was too small to estimate reliably from the data. This agrees with the large resistance predicted by our numerical model. In contrast, the current in tap water was dominated by the conductive component, while the fitted capacitive contribution was also too small to estimate. This is again consistent with the much lower resistance expected for tap water. The fitted circuit parameters are summarized in Table 4.3.

Water type	Resistance R	Capacitance C
DI water	-	41 pF
Tap water	444 Ω	-

Table 4.3: Equivalent circuit parameters obtained from a fit .

For both the resistance of the tap water and the capacitance of the DI water, the fitted values differ from the numerical prediction by approximately a factor of two, which verifies our model is approximately correct.

The chosen simplified equivalent circuit model is also justified as, the fitted current follows the measured waveform well. This is except near the moment when the polarity of the high voltage pulse changes. This effect is especially visible for DI water. A possible explanation is the accumulation of surface charge at the water–air interface. These charges effectively behave as an additional temporary capacitance, which must first discharge and then recharge with opposite polarity when the applied voltage changes sign.

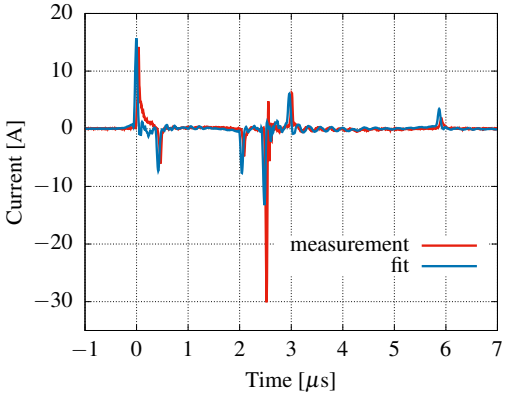


Figure 4.6: Fit of the measured discharge in deionized water by the equivalent circuit.

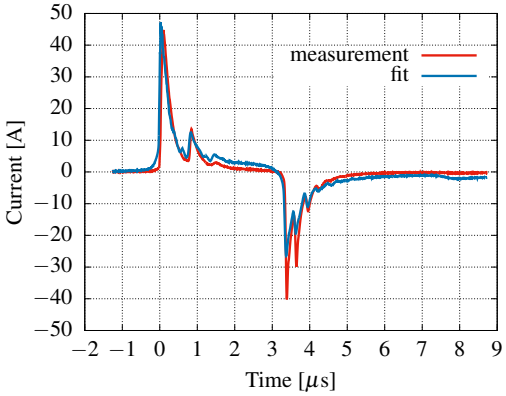


Figure 4.7: Fit of the measured discharge in tap water by the equivalent circuit.

4.1.3 Heating model

In this section, we estimate the energy deposited into the water by conductive current heating pulse. The resistive power density is determined from the electric field distribution and integrated over the volume. The is calculated as

$$P(t) = 2d\,\sigma \int E(t)^2\,dS, \tag{4.3}$$

where d is the electrode depth, σ is the electrical conductivity of water, and $E(t)$ is the electric field magnitude. Equivalently, having calculated the approximate resistance we have $P = U^2/R$. The total energy deposited during one pulse can be written as

$$W = \int P(t)\,dt. \tag{4.4}$$

The calculated energy per pulse is summarized in Table 4.4. To estimate the average deposited power we also need the pulse repetition frequency. The experiments in Arora et al. [5]used repetition frequencies of 2 Hz for imaging measurements and 20 Hz for optical emission spectroscopy. The system contained approximately 5 L of circulating water, corresponding to a heat capacity of roughly 21 $\mathrm{kJ\,K^{-1}}$. Compared to this value, the estimated Joule heating from the conductive current is almost insignificant. We can also calculate the total available energy in each pulse from the measured current and voltage as

$P = UI$. Integrating this over the pulse, we will find energy on the same order of tens of Jouls at most. The heating of the water is therefore a very small effect.

Water type	Conductivity [S m^{-1}]	Energy per pulse [J]
DI water	1.2×10^{-4}	1.2×10^{-3}
Tap water	4.5×10^{-2}	5.0×10^{-1}

Table 4.4: Estimated energy deposited into water during one pulse.

4.2 Convergence and error analysis

To asses the reliability of our solution, we compute the global a posteriori error estimator η_h under uniform refinement as described in the previous section. The results shown in Fig. 4.8 show, that the solution does not achieve the theoretical convergence rates $\mathcal{O}(h^{k+1})$ observed in the manufactured test cases. Specifically, while the 0th order elements behave as expected, the 1st and 2nd order elements show significant degradation in convergence slopes.

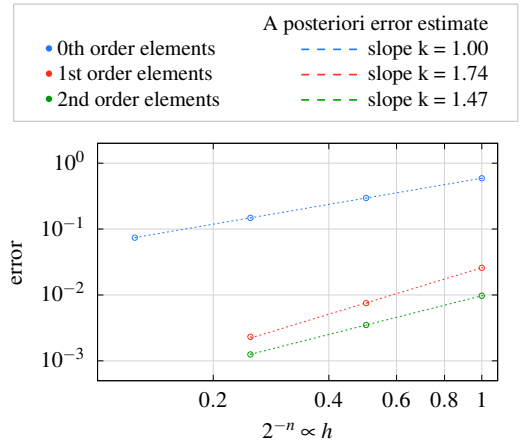


Figure 4.8: Convergence of the A posteriori error estimator

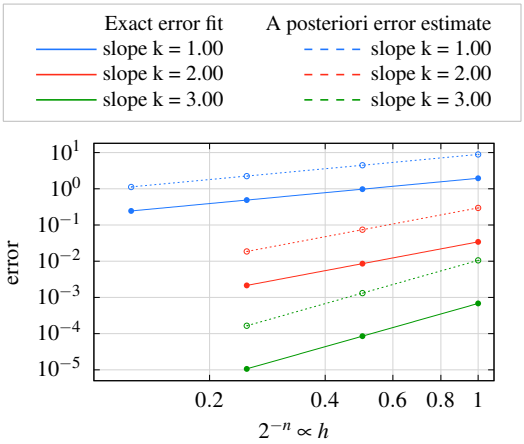


Figure 4.9: Convergence on reactor triangulation with manufactured solution

There are two primary factors that could cause such degradation: geometric distortion of the elements (mesh quality) or insufficient regularity of the exact solution. To isolate the cause, we tried to compute again using our manufactured solution onto the same reactor triangulation. As shown in Fig. 4.9, the estimator recovers the ideal convergence rates. This proves that the triangulation itself has sufficient quality.

To investigate further, we plot the error estimate for each cell on an unrefined mesh in Fig. 4.10 and Fig. 4.11. The highest values of the error can be observed primarily around curved physical boundaries with a jump in ε or curved outer boundaries. This is what is expected as around those regions the displacement field D will spike. The error is of course also high on large elements, because in that case it accumulates over a larger area even though the local error is relatively small.

For these reasons, we believe that the lack of convergence in the physical problem is a result of the low regularity of the solution and can't be mitigated. The error estimate is however still expected to provide a reliable measure of convergence.

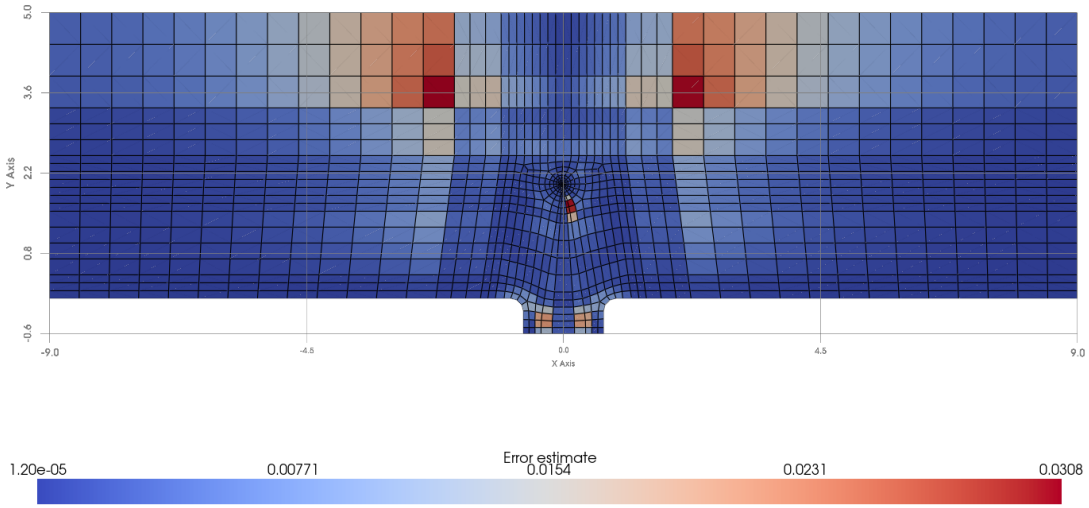


Figure 4.10: The calculated error estimate per cell.

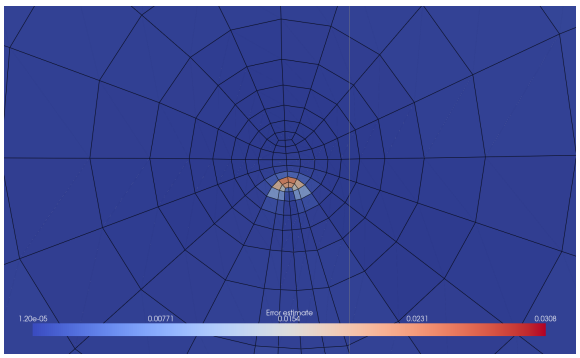
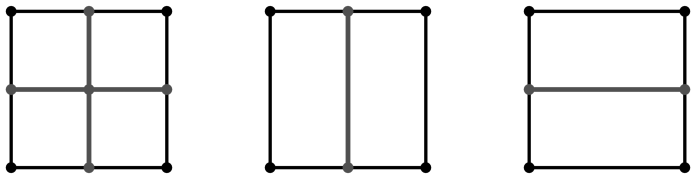


Figure 4.11: The calculated error estimate per cell near the blade region.

4.2.1 Anisotropic adaptive refinement

In this section we extend the adaptive refinement strategy introduced for the test case, which was based on isotropic refinement of cells. In that case we cut all edges in half and form new cells from these edges, also possibly placing the newly formed vertices according to the underlying geometry. Anisotropic refinement refers to the process of splitting only along one of the edges as illustrated on Fig. 4.12.



Isotropic ξ-direction η-direction

Figure 4.12: Comparison of refinement strategies

The benefits of this approach are two fold. Often, when the solution has very directional features, it is much more favorable to increase resolution only in this direction. Anisotropic refinement can therefore lead to a more efficient mesh approximation of these features. The other added benefit, is that the aspect ratio of cells can change by a factor of 2 at each step. If there are any cells, that become excessively thin with refinement, because of curved edges or other reasons, their aspect ratio can be improved.

To take advantage of this refinement strategy, we need a directional indicator of the error. By examining the a posteriori error (2.28), which is cited here again, we see that there are coupled terms, which can't be reasonably split into directional parts such as the curl and divergence terms.

$$\begin{aligned}\eta_T^2 =& \|\rho - \nabla\cdot\vec{D}_h\|^2_{L^2(T)} + h_T^2\|\nabla\times(\varepsilon^{-1}\vec{D}_h)\|^2_{L^2(T)}\\ &+ h_T^2\|\varepsilon^{-1}\vec{D}_h + \nabla\phi_h\|^2_{L^2(T)} + \|h_E^{1/2}J(\varepsilon^{-1}\vec{D}_h\cdot\vec{t})\|^2_{L^2(\partial T)}\end{aligned}$$

We will group those into the direction independent part of the error

$$\eta_{\xi\eta}^2 = \|\rho - \nabla\cdot\vec{D}_h\|^2_{L^2(T)} + h_T^2\|\nabla\times(\varepsilon^{-1}\vec{D}_h)\|^2_{L^2(T)}. \tag{4.5}$$

This contribution is split equally between the two local directions. The remaining terms can be decomposed directionally. The residual $\vec{R} = \varepsilon^{-1}\vec{D}_h + \nabla\phi_h$ is projected onto the local coordinate system, and the jump term naturally separates according to the orientation of the cell faces (see Fig. 4.13). The resulting directional error indicators for a cell T are then given by:

$$\eta_\xi^2 = 0.5\eta_{\xi\eta}^2 + h_T^2\|\vec{R}\cdot\hat{\xi}\|^2_{L^2(T)} + \|h_E^{1/2}J(\varepsilon^{-1}\vec{D}_h\cdot\vec{t})\|^2_{L^2(\partial T_\xi)} \tag{4.6}$$

$$\eta_\eta^2 = 0.5\eta_{\xi\eta}^2 + h_T^2\|\vec{R}\cdot\hat{\eta}\|^2_{L^2(T)} + \|h_E^{1/2}J(\varepsilon^{-1}\vec{D}_h\cdot\vec{t})\|^2_{L^2(\partial T_\eta)} \tag{4.7}$$

The refinement strategy then follows the same idea as before. All directional error indicators η_ξ and η_η are sorted, and a fixed fraction (for example the top 50%) is marked for refinement. If both directional indicators of a cell are marked, the cell is refined isotropically. Otherwise, refinement is applied only in the direction corresponding to the larger error.

The resulting mesh after four refinement steps is shown in Fig. 4.14. One can notice that many of the relatively thin rectangular cells in the outer regions of the initial mesh have

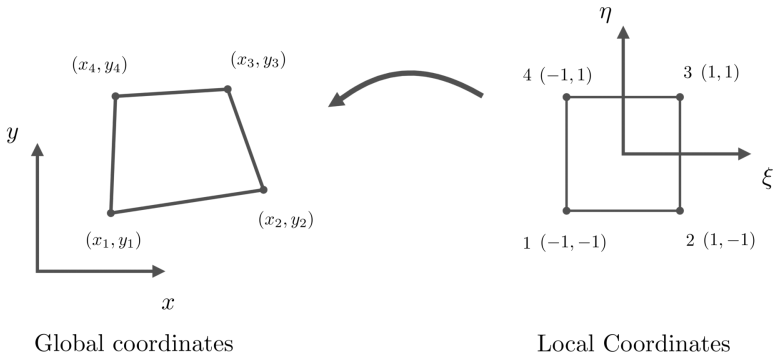


Figure 4.13: Local to global coordintaes

been refined into square elements. This is exactly the benefit that was already mentioned, that aspect ratios of elements can change due to refinement. When constructing the mesh originally, we started from a fairly fine structured regular grid and then as a final step a lot of the outer edge loops were removed to reduce the overall mesh complexity of the base mesh. This simplification introduced the elongated cells in some regions. With anisotropic refinement, these regions are naturally refined back to the underlying square grid, but only as far as it's computationally efficient.

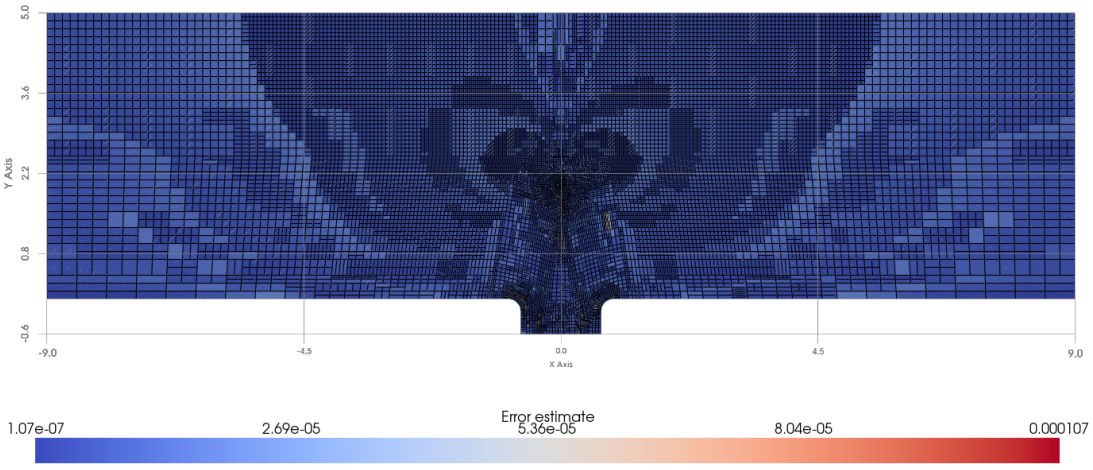


Figure 4.14: Final mesh after four anisotropic refinement steps with 50% marking.

Chapter 5

Conclusion

In this thesis we studied the electric field and conductive heating in a plasma–liquid reactor using numerical simulation based on the finite element method.

The work first described the main physical processes that occur near the water–air interface, where the electrical discharge is formed. The reactor geometry and operating conditions were taken from published experimental studies. Based on this, a simplified electrostatic model of the reactor was created.

The simulations showed how the reactor geometry influences the electric field distribution near the water–air interface. An insulating blade inside the reactor changes the local electric field enough to create conditions needed for discharge to form above the liquid surface. This agrees with experimental observations, where the discharge appears in the same area.

The model was also used to estimate Joule heating in the liquid caused by conductive currents. The results showed that the amount of deposited energy strongly depends on the electrical conductivity of the water. In deionized water, the heating effect was very small, while in tap water the deposited energy was much larger because the conductivity is higher.

The numerical implementation was verified by convergence analysis, and the obtained results were physically reasonable and consistent with the expected behaviour of the reactor.

The model used in this work is simplified and does not include effects such as plasma chemistry, charge transport, or time-dependent discharge dynamics. It is however a basis for a more complete plasma–liquid model that could include these effects in future work.

Literature

[1] P. J. Bruggeman, M. J. Kushner, B. R. Locke, *et al.*, "Plasma–liquid interactions: A review and roadmap," *Plasma Sources Science and Technology*, vol. 25, no. 5, p. 053 002, Sep. 2016. DOI: 10.1088/0963-0252/25/5/053002. [Online]. Available: https://doi.org/10.1088/0963-0252/25/5/053002.

[2] I. Adamovich, S. Agarwal, E. Ahedo, *et al.*, "The 2022 plasma roadmap: Low temperature plasma science and technology," *Journal of Physics D: Applied Physics*, vol. 55, no. 37, p. 373 001, Jul. 2022. DOI: 10.1088/1361-6463/ac5e1c. [Online]. Available: https://doi.org/10.1088/1361-6463/ac5e1c.

[3] P. Ranieri, N. Sponsel, J. Kizer, *et al.*, "Plasma agriculture: Review from the perspective of the plant and its ecosystem," *Plasma Processes and Polymers*, vol. 18, no. 1, p. 2 000 162, 2021. DOI: https://doi.org/10.1002/ppap.202000162. eprint: https://onlinelibrary.wiley.com/doi/pdf/10.1002/ppap.202000162. [Online]. Available: https://onlinelibrary.wiley.com/doi/abs/10.1002/ppap.202000162.

[4] P. Hoffer, V. Prukner, G. Arora, and M. Šimek, "High-speed imaging reveals the dynamics of the initiation and subsequent evolution of a nanosecond discharge propagating along the air–water interface," *Plasma Sources Science and Technology*, vol. 32, no. 9, 09LT01, Oct. 2023. DOI: 10.1088/1361-6595/acf955. [Online]. Available: https://doi.org/10.1088/1361-6595/acf955.

[5] G. Arora, P. Hoffer, V. Prukner, P. Bílek, and M. Šimek, "Properties and characteristics of the nanosecond discharge developing at the water–air interface: Tracking evolution from a diffused streamer to a spark filament," *Plasma Sources Science and Technology*, vol. 33, no. 2, p. 025 025, Feb. 2024. DOI: 10.1088/1361-6595/ad257d. [Online]. Available: https://doi.org/10.1088/1361-6595/ad257d.

[6] D. Arndt, W. Bangerth, M. Bergbauer, *et al.*, "The deal.ii library, version 9.7," *Journal of Numerical Mathematics*, vol. 33, no. 4, pp. 403–415, 2025. DOI: 10.1515/jnma-2025-0115.

[7] D. Boffi, F. Brezzi, and M. Fortin, *Mixed Finite Element Methods and Applications* (Springer Series in Computational Mathematics). Springer, 2013, vol. 44. DOI: 10.1007/978-3-642-36519-5.

[8] C. Carstensen, "A posteriori error estimate for the mixed finite element method," *Mathematics of Computation*, vol. 66, no. 218, pp. 465–476, 1997. DOI: 10.1090/S0025-5718-97-00837-5.